Journal of Materials Chemistry C

ROYAL SOCIETY OF CHEMISTRY

PAPER

Check for updates

Cite this: J. Mater. Chem. C, 2021, 9, 16945

The intrinsic thermal transport properties of the biphenylene network and the influence of hydrogenation: a first-principles study†

Pei Zhang, [a] Tao Ouyang, *[a] Chao Tang,*[a] Chaoyu He,[a] Jin Li, [a] Chunxiao Zhang, [a] Ming Hu *[b] and Jianxin Zhong[a]

Received 2nd September 2021, Accepted 28th October 2021

DOI: 10.1039/d1tc04154a

rsc.li/materials-c

Utilizing first-principles calculations combined with phonon Boltzmann transport theory up to fourth-order anharmonicity, we systematically investigate the thermal transport properties of the biphenylene network [BPN, recently synthesized experimentally by Fan *et al.*, *Science*, 2021, **372**, 852–856] and hydrogenated BPN (HBPN). The calculations show that four-phonon scattering significantly affects the lattice thermal conductivity (κ) of BPN. At room temperature, the κ of BPN is reduced from 582.32 (1257.07) W m^{-1} K^{-1} to 309.56 (539.88) W m^{-1} K^{-1} along the x (y) direction after considering the four-phonon scattering. Moreover, our results demonstrate that the thermal transport in BPN could also be greatly suppressed by hydrogenation, where the κ of HBPN along the x (y) direction is merely 16.62% (10.14%) of that of pristine BPN at 300 K. The mechanism causing such an obvious decrease of κ of HBPN is identified to be due to the enhanced phonon scattering rate and reduced group velocity, which is further revealed by the increased scattering phase space and weakened C–C bond. The results presented in this work shed light on the intrinsic thermal transport features of BPN and HBPN, which will help us to understand the phonon transport processes and pave the way for their future developments in the thermal field.

1. Introduction

Carbon materials occupy a crucial position in the development of science and technology due to their unique properties and rich variety of allotropes.[1–6] Since the discovery of monolayer graphene,[5] two-dimensional (2D) carbon materials have received extensive attention[7–9] and numerous new 2D carbon allotropes with rich electronic properties have been predicted and reported. For instance, net W,[10] R-graphyne,[11] ψ-graphene,[12] and net-τ[13] feature metallic characteristics, while graphenylene,[14] penta-graphene,[15] twin graphene,[16] and C68-graphyne[17] are semiconductors with different band gaps. More interestingly, OPG-Z,[18] phagraphene,[19] Stone–Wales graphene,[20] and SW40[21] are semimetals with topological properties. In addition to the advances in theory, great effort has also been made in the experimental synthesis of 2D carbon materials. Large-area graphdiyne film has been prepared by a cross-coupling reaction of hexaethylbenzene.[22] Using an on-surface reaction approach, phagraphene and TPH-graphene have been obtained as well.[23] Recently, the biphenylene network (BPN), a previously predicted graphene allotrope with metallic properties, has been realized *via* an on-surface interpolymer dehydrofluorination reaction by Fan *et al.*[24] These advancements illustrate that 2D carbon structures never cease to inspire the enthusiasm and creativity of researchers.

Thermal transport is a fundamental physical property of materials and is essential for practical applications, such as thermal dissipation in electronic devices and heat hindering in thermoelectrics. Various thermal transport properties have been reported in 2D carbon allotropes, which has stimulated a wide range of research interests. The suspended graphene possesses a superb thermal conductivity (κ) of over 3000 W m^{-1} K^{-1} at room temperature. Other 2D carbon structures with similar planar configurations, however, display different thermal transport behaviors. For example, the κ of penta-graphene is about 645 W m^{-1} K^{-1},[25] and that of γ-graphyne with sp and sp^2 hybrid states is merely 76 W m^{-1} K^{-1} which is two orders of magnitude lower than that of graphene at 300 K.[26] These results indicate that the geometric structure and C–C bond type have an important influence on the κ of the 2D carbon allotropes. Meanwhile, it is also vital to modulate the κ to meet the needs of a variety of different application requirements. Several

[a] Hunan Key Laboratory for Micro-Nano Energy Materials & Device and School of Physics and Optoelectronics, Xiangtan University, Xiangtan 411105, Hunan, China. E-mail: ouyangtao@xtu.edu.cn, tang_chao@xtu.edu.cn

[b] Department of Mechanical Engineering, University of South Carolina, Columbia, SC 29208, USA. E-mail: hu@sc.edu

† Electronic supplementary information (ESI) available. See DOI: 10.1039/d1tc04154a

methods have been developed to effectively regulate the κ, *e.g.* nanostructuring,[27,28] introduction of pores and impurities,[29,30] and strain.[31–33] Among the various methods, recent studies on hydrogenated graphene and penta-graphene have demonstrated that hydrogenation is also a feasible way to adjust the κ of 2D materials.[34,35] Considering the peculiar configuration arranged with tetragonal, hexagonal, and octagonal carbon rings in a recently prepared BPN,[24] it is natural to ask how its distorted sp^2 hybridization bonds will affect its intrinsic thermal conductivity. How could hydrogenation modulate its thermal conductivity?

To answer these questions, in this work, we systematically investigate the κ of BPN and hydrogenated BPN (HBPN) by means of first-principles combined with phonon Boltzmann transport theory by considering both three- and four-phonon scattering. The calculations show that the four-phonon scattering plays a significant role in the intrinsic thermal transport properties of BPN and HBPN. Meanwhile, we also find that hydrogenation not only weakens the anisotropy of thermal conductivity and phonon hydrodynamics of BPN and shortens the phonon mean free path as well, but also leads to a significant decrease in κ. The rest of this paper is organized as follows. In Section 2, a brief description of computational details of first-principles and Boltzmann transport theory is presented. In Section 3, we show the main calculation results and discuss in detail the κ of BPN and HBPN based on the phonon scattering rate, group velocity, scattering phase space, and hybridization orbitals of electrons. Finally, the conclusions of this work are given in Section 4.

2. Materials and methods

The first-principles calculations are carried out by density functional theory employing the projector augmented wave (PAW) pseudopotential in the Vienna *ab initio* simulation package (VASP).[36–38] The exchange–correlation functional adopts the Perdew–Burke–Ernzerhof (PBE) generalized gradient approximation (GGA).[39] Both BPN and HBPN use a plane wave basis with a cutoff energy of 550 eV, and their Brillouin zone (BZ) is sampled using $7 \times 8 \times 1$ and $7 \times 7 \times 1$ Monkhorst–Pack *k*-meshes, respectively. The energy and Hellmann–Feynman force convergence criteria are set to 10^{-6} eV and 10^{-4} eV Å^{-1}, respectively. A vacuum region of more than 15 Å is applied for avoiding layer-to-layer interactions caused by periodic boundary conditions.

The harmonic second-order force constants and phonon spectra are computed by using VASP and PHONOPY software.[40] The anharmonic third-order force constants are generated by the thirdorder.py script and interaction up to the sixth nearest neighbors is employed.[41] The fourthorder.py code is utilized to obtain the anharmonic fourth-order force constants,[42] and we consider the interaction up to the second nearest neighbors. The real-space finite-difference method and same supercell sizes are used to calculate the harmonic and anharmonic force constants, *i.e.*, $3 \times 4 \times 1$ and $2 \times 2 \times 1$ supercells are taken for BPN and HBPN, respectively. We adopt the thickness of 3.35 Å and 5.3 Å for BPN and HBPN by considering the van der Waals radius, respectively. Based on the physical quantities obtained above, the phonon transport properties of BPN and HBPN are obtained *via* the ShengBTE software package.[43] The phonon thermal conductivity is defined as[43]

$$\kappa_\alpha = \sum_\lambda c_\lambda v_{\lambda,\alpha}\left[\tau_\lambda^0\left(v_{\lambda,\alpha} + \Delta_\lambda\right)\right], \quad (1)$$

where c_λ, $v_{\lambda,\alpha}$, τ_λ^0 and Δ_λ denote specific heat, phonon group velocity along the α direction, phonon relaxation time, and correction term with the dimension of velocity, respectively, and the subscript $\lambda \equiv (q, p)$ is the sum of all phonon modes in the Brillouin zone, where q and p are the phonon wave vectors and mode indices. Both three-phonon and four-phonon scattering rates ($1/\tau_\lambda$) are considered in this work. In order to get the convergence of the thermal conductivity, phonon q-grid points of $36 \times 45 \times 1$ ($16 \times 20 \times 1$) and $20 \times 20 \times 1$ ($6 \times 6 \times 1$) are chosen for BPN and HBPN for considering the three-phonon (four-phonon) scattering rate, respectively (the convergence results are depicted in Fig. S1 and S2 of the ESI†).

3. Results and discussion

Firstly, we give the structural information about the BPN and HBPN, where the top and side views of both BPN and HBPN are illustrated in Fig. 1. It can be seen that the BPN possesses six carbon atoms in each primitive cell, it consists of four-, six- and eight-membered carbon rings and the optimized lattice constants of BPN are a = 4.52 Å and b = 3.76 Å, which agree well with previous theoretical and experimental results.[24,44] The ground state configuration of the HBPN sheet is determined by using the powerful structure search software RG2 code.[45] Detailed information about searching for HBPN sheets can be found in our recent work.[46] After the hydrogenation of BPN, the space group changes from *Pmmm* (No. 47) to *Cmma* (No. 67). Differently from BPN, the HBPN hosts 24 atoms (12 carbon

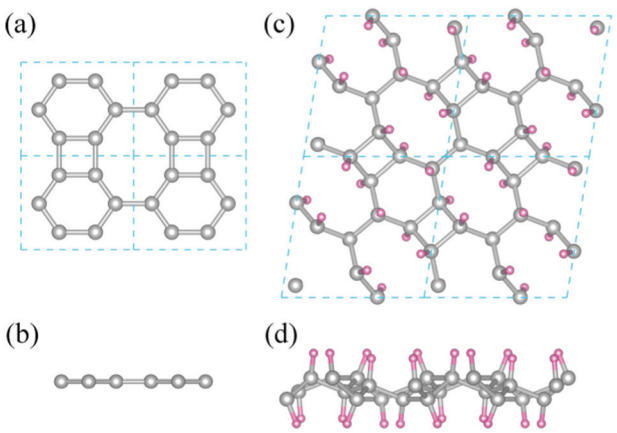

Fig. 1 Top and side views of (a and b) the biphenylene network (BPN) and (c and d) the hydrogenated biphenylene network (HBPN). The gray and red balls denote carbon and hydrogen atoms, respectively. The blue dashed boxes in (a and c) indicate the primitive cells.

 This journal is © The Royal Society of Chemistry 2021

atoms and 12 hydrogen atoms) in each primitive cell. The optimized lattice constant of HBPN is $a = b = 5.86$ Å. As shown in Fig. 1(c) and (d), it is obvious that when the BPN is hydrogenated, the planar structure turns into a buckled configuration due to the variation of the orbital hybridization form. It should be also pointed out that hydrogenation does not destroy the original C–C bond and modifies the basic atomic framework of BPN (the carbon atoms are still arranged in four, six, and eight-membered rings). However, such behavior leads to a notable difference in the electronic band structures between BPN and HBPN, *i.e.*, the BPN is transformed from metal to insulator after hydrogenation, and the band gap of HBPN is about 4.65 eV based on the HSE06 potential (more information could be found in Fig. S3 of the ESI†).

Based on the optimized structure, we analyze the phonon dispersion relations to verify the dynamical stability of BPN and HBPN. Their corresponding phonon spectra and phonon density of states (pDOS) are depicted in Fig. 2. The phonon spectra of both BPN and HBPN are free of imaginary frequencies, indicating that they are dynamically stable in the ground state. One can also find that the phonon branches in BPN become more numerous and denser after hydrogenation, which leads to a larger pDOS. In addition, the cutoff frequency of optical phonon branches of HBPN is 89.22 THz, which is much larger than that of BPN (49.34 THz) and mainly originated from the light mass of hydrogen atoms. However, it is worth mentioning

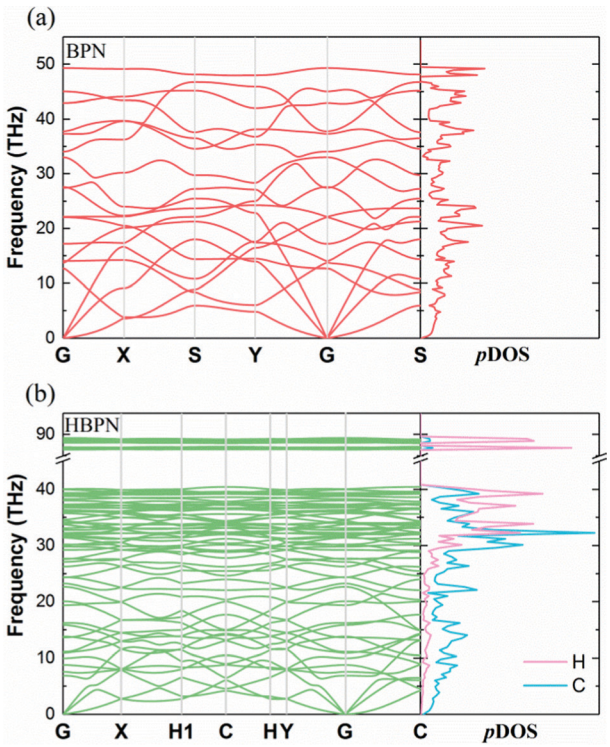

Fig. 2 The phonon dispersions curve and phonon density of states (pDOS) of (a) BPN and (b) HBPN. For HBPN, the atom partial DOS are plotted. The coordinates of the high-symmetry points in the Brillouin zone are *G* (0, 0, 0), *X* (0.5, 0, 0), *S* (0.5, 0.5, 0), *Y* (0, 0.5, 0), *H*1 (0.865, 0.433, 0), *C* (0.5, 0.5, 0), and *H* (0.135, 0.568, 0).

that the phonon branches of HBPN are significantly softened in the low frequency region (less than 40 THz). From the partial DOS shown in Fig. 2(b), it can be noted that the phonons in the low-frequency region are mainly contributed by C atoms, while the contribution from H atoms is mainly in the high-frequency phonon region. The behavior of these phonon branches will play a critical role in phonon transport, which will be discussed in the following.

In Fig. 3(a) and (b), we plot the lattice thermal conductivity as a function of temperature for both BPN and HBPN. Here, we carry out the three-phonon (3-phonon) scattering computation using the iterative method. As for the four-phonon (4-phonon) scattering processes, we utilize the relaxation time approximation (RTA) approach because the iterative way will demand large calculation resources (processor and memory), which is a common treatment for the high-order anharmonic phonon scattering calculations.[42] Since the ascent of temperature will strengthen the Umklapp phonon–phonon scattering, it can be seen that the κ value of both BPN and HBPN decreases with increasing temperature, which is a typical behavior of crystalline materials.[47–49] Meanwhile, one can notice that after including the 4-phonon scattering κ is far lower than that where only 3-phonon scattering is considered. For instance, at room temperature, the κ value along the x (y) direction for BPN decreases from 582.32 (1257.07) W m^{-1} K^{-1} to 309.56 (539.88) W m^{-1} K^{-1}, by 46.84% (57.05%). Analogous phenomena could also be found in the HBPN. Such reduction in κ could be easily understood from the enhancement of the scattering rate shown in Fig. 4(a and b). It should be mentioned here that our calculated thermal conductivity (only with 3-phonon scattering) of BPN is larger than the results reported in recent work.[44] The discrepancy might be attributed to the different supercell sizes and cutoff radius for obtaining the harmonic and anharmonic force constants. We also notice the large anisotropy in the phonon transport of BPN, *i.e.* the κ^{3+4ph} along the y direction is 1.74 times higher than that along the x direction, which is mainly caused by the anisotropic structure of the BPN. In addition, it can be viewed from Fig. S4 (ESI†) that the discrepancy between the thermal conductivity of the BPN obtained using the iterative and RTA methods is significant. At room temperature, the difference factor $(1 - \kappa^{3ph}_{RTA}/\kappa^{3ph}_{Iterative})$ along the x (y) direction is 0.48 (0.47). Such a large difference factor suggests the possible existence of phonon hydrodynamics in BPN, which is also observed in graphene.[50]

Another significant result presented in Fig. 3(a and b) is that after the BPN is hydrogenated to HBPN, its thermal conductivity is greatly suppressed. The room temperature κ^{3+4ph} of HBPN along the x (y) direction is merely 51.46 (54.73) W m^{-1} K^{-1}, which is only 16.62% (10.14%) of that of BPN. Besides, the anisotropic thermal transport in BPN disappeared as well in HBPN, where the anisotropic factor $[|\kappa_x^{3+4ph} - \kappa_y^{3+4ph}|/(\kappa_x^{3+4ph} + \kappa_y^{3+4ph})]$ decreases from 0.27 to 0.03 at 300 K. Interestingly, it can also be seen from Fig. S4(c) (ESI†) that the difference factor of HBPN is much smaller than that of BPN, *e.g.*, at room temperature, the difference factor of HBPN is only 0.05 (0.04) along the x (y) direction. Such variation implies that

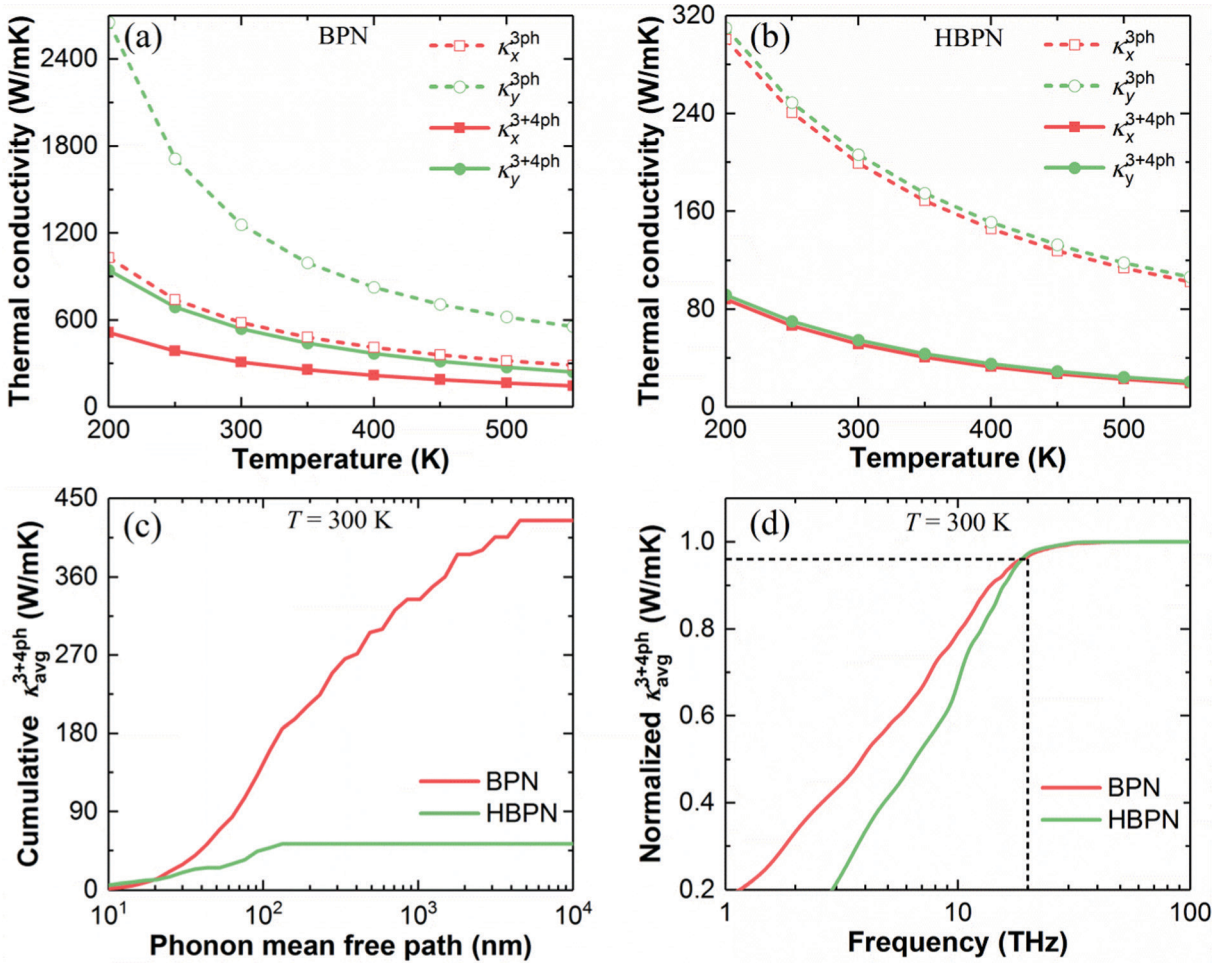

Fig. 3 Thermal conductivity *versus* temperature for (a) BPN and (b) BPN along the *x* and *y* directions. 3ph and 3 + 4ph denote only three-phonon scattering and both three-phonon and four-phonon scattering, respectively. (c) Cumulative κ_{avg}^{3+4ph} as a function of phonon mean free path. (d) Normalized cumulative κ_{avg}^{3+4ph} as a function of frequency.

hydrogenation may reduce the phonon hydrodynamics of BPN as well. For showing the effect of hydrogenation on the thermal conductivity of BPN more clearly, the cumulative averaged thermal conductivity $[\kappa_{avg}^{3+4ph} = (\kappa_x^{3+4ph} + \kappa_y^{3+4ph})/2]$ as a function of the phonon mean free path (PMFP) at room temperature is depicted in Fig. 3(c). It is evident that their κ_{avg}^{3+4ph} value at first increases with the PMFP and then converges to a constant value of 424.72 W m^{-1} K^{-1} and 53.10 W m^{-1} K^{-1} for BPN and HBPN, respectively. Moreover, one can find that hydrogenation also causes a reduction in the PMFP, with the maximum PMFP falling from 4534.88 nm for BPN reduce to 132.19 nm for HBPN. This indicates that nanostructuring might be a more effective way to modulate the thermal conductivity of HBPN. Finally, we also give the κ_{avg}^{3+4ph} as a function of phonon frequency. It can be noted from Fig. 3(d) that most of the κ_{avg}^{3+4ph} is contributed by phonons with frequencies below 20 THz for both BPN and HBPN.

To explore the physical mechanism of the evident reduction of κ_{avg}^{3+4ph} of HBPN, we decompose the phonon properties that influence the κ, *i.e.*, specific heat (C_λ), phonon scattering rate ($1/\tau_\lambda$), and phonon group velocity (v_λ). Since the softening of phonon modes after hydrogenation leads to more phonon modes per unit frequency, as listed in Table 1, the specific heat of HBPN is greater than that of BPN. That is to say, the elevated specific heat is not responsible for the lower κ of HBPN. As for the phonon scattering rate, it can be seen from Fig. 4(a and b) that the phonon scattering rate of HBPN is much larger than that of BPN. In other words, the phonon relaxation time is reduced, which is one of the reasons for the decrease of κ_{avg}^{3+4ph} after hydrogenation.

The phonon scattering rate is determined by two factors, one of which is the amount of phonon scattering channels, determined by the 3-phonon and 4-phonon scattering phase space. The other is the intensity of phonon scattering, which is quantified by the Grüneisen parameter. As one can observe in Fig. 4(c), the hydrogenation boosts the 3-phonon (phonon frequency <10 THz) and 4-phonon (phonon frequency $>$ 10 THz) scattering phase space. Such enhancement originates from the fact that the increased and softened phonon branches caused by hydrogenation make it easier for phonons to satisfy energy and quasi-momentum conservation, thereby allowing more channels for phonons to be scattered. Nevertheless, the

 This journal is © The Royal Society of Chemistry 2021

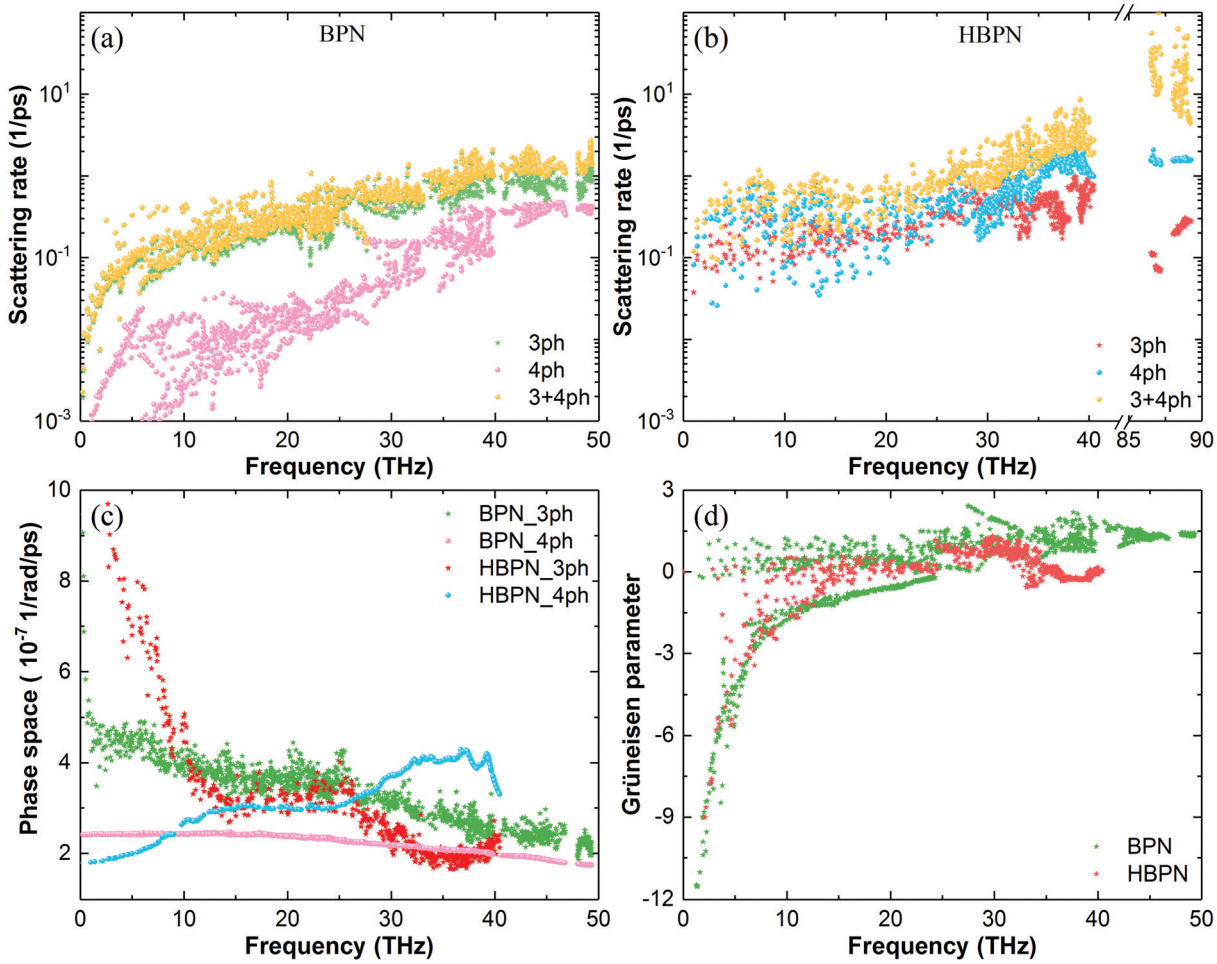

Fig. 4 At room temperature, comparison of phonon scattering rate of (a) BPN and (b) HBPN. 3ph, 4ph, and 3 + 4ph denote only 3-phonon scattering, 4-phonon scattering, and both 3-phonon and 4-phonon scattering, respectively. (c) 3-Phonon and 4-phonon scattering phase space of BPN and HBPN. (d) Grüneisen parameter of BPN and HBPN.

Table 1 The specific heat of BPN and HBPN

Material	BPN	HBPN
Specific heat (kJ m^{-3} K^{-1})	281.12	367.73

Grüneisen parameter (absolute value) of the HBPN is lower than that of the BPN as depicted in Fig. 4(d), indicating a weaker anharmonicity of the HBPN. It is evident that the reduction in anharmonicity cannot explain the increasing phonon scattering rate of HBPN with respect to BPN. Therefore, one can conclude that it is mainly the enhancement of the scattering phase space that causes the increase of phonon scattering rate of HBPN compared to BPN.

According to eqn (1), the phonon group velocity is the other key factor affecting the κ value. It is clearly seen from Fig. 5(a) that the group velocity of HBPN is reduced compared to that of BPN. The maximum phonon group velocity of BPN is 19.53 km s^{-1} and that of HBPN is only 13.37 km s^{-1}, and the smaller group velocity is consistent with the lower Young's modulus (Table S1, ESI†). Such reduction is attributed to the softening of phonon branches with frequencies less than 40 THz mentioned earlier since group velocity is the slope of the phonon branch. As all the properties are substantially dependent on the atomic structure and electronic properties, we further investigate the group velocity from the viewpoint of bond strength. One can notice from Fig. 5(b and c) and Fig. S3(b) (ESI†) that the carbon atoms in BPN are bonded to only three adjacent carbon atoms and therefore form sp^2 hybridization orbitals, while the p_z orbitals are not involved in hybridization and form π-bonds. After hydrogenation, the previously unhybridized p_z orbital of the carbon atom hybridizes with the s orbital of the hydrogen atom to form the sp^3 hybridization orbital (Fig. S3(d), ESI†), which induces the buckled structure of HBPN. In general, the fewer the "s" properties of a material, the weaker its bond energy will be.[35,51] Therefore, the strength of the C–C bond becomes weaker after hydrogenation, as evidenced by the trace of the harmonic force constant in Table S2 in the ESI.† At the same time, the electron local function (ELF) could also demonstrate the bonding properties visually. The electrons previously in the unhybridized p_z orbital of BPN are currently localized on the

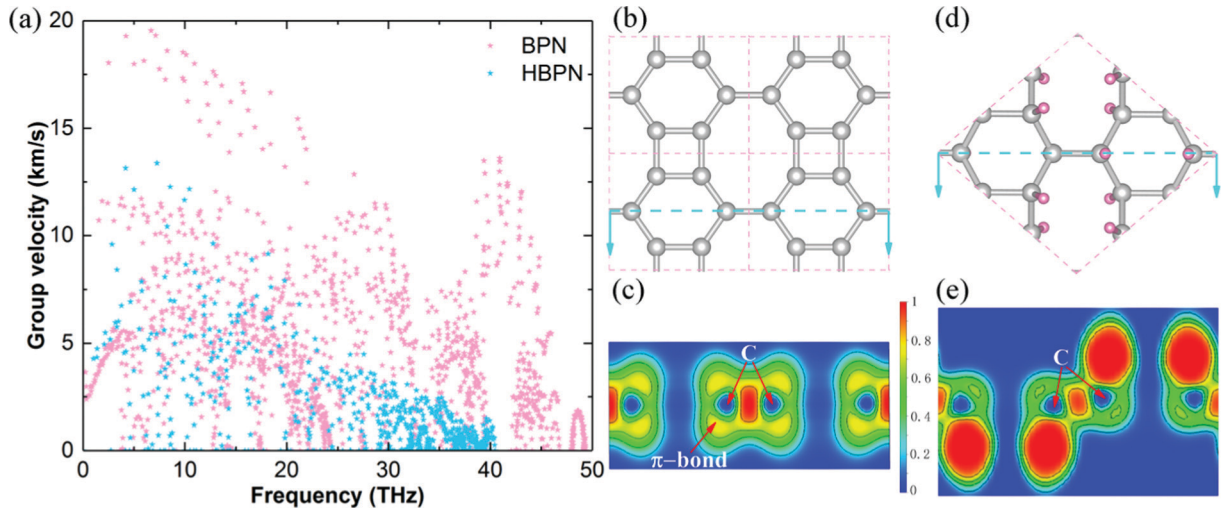

Fig. 5 (a) Comparison of phonon group velocity of BPN and HBPN. (b and c) Atomic structures of BPN and HBPN, the blue dashed line indicates the cross-section of the electron localization function (ELF). (d and e) ELF of BPN and HBPN. The two bonded carbon atoms are denoted by "C".

C–H bond [large red areas in Fig. 5(e)] and hence are not involved in C–C formation anymore. As a result, it is the weakening of the C–C bond that leads to the decrease of the group velocity of HBPN relative to BPN.

4. Conclusion

In summary, by combining the first-principles calculations with the Boltzmann transport theory, we systematically investigated the thermal transport properties of BPN and HBPN. Since higher-order phonon scattering plays an important role in more accurate calculations of the thermal conductivity of materials, four-phonon scattering is also considered in our work. The calculations show that the thermal conductivity of BPN decreases by 46.84% (57.05%) along the x (y) direction because of the increase in the scattering rate, after considering the four-phonon scattering. Meanwhile, another important result indicates that hydrogenation not only weakens the anisotropy of thermal conductivity and phonon hydrodynamics of BPN, and shortens the PMFP as well, but also leads to a significant decrease in κ_{avg}^{3+4ph}. At room temperature, the κ_{avg}^{3+4ph} of HBPN is merely 51.46 (54.73) W m^{-1} K^{-1}, which is about 16.62% (10.14%) of that of BPN. Through analysis of phonon mode performance, one can find that both the phonon scattering rate and group velocity are responsible for the decrease of κ_{avg}^{3+4ph} after hydrogenation of BPN, which is further attributed to the enlarged scattering phase space (including the 3-phonon and 4-phonons) and the weaker C–C bond. Our calculations shed light on the inherent phonon transport characteristics of BPN and the effect of hydrogenation and provide theoretical guidance for potential applications of BPN and HBPN.

Author contributions

Pei Zhang: data curation, formal analysis, investigation, visualization, writing – original draft, writing – review & editing, funding acquisition. Tao Ouyang: conceptualization, methodology, supervision, validation, funding acquisition, writing – review & editing. Chao Tang: resources, software, discussion, writing – review & editing. Chaoyu He: discussion, writing – review & editing. Jin Li: discussion, writing – review & editing. Chunxiao Zhang: discussion, writing – review & editing. Ming Hu: conceptualization, validation, discussion, funding acquisition, writing – review & editing. Jianxin Zhong: discussion, funding acquisition, writing – review & editing.

Conflicts of interest

The authors declare that they have no known competing financial interests or personal relationships that could have appeared to influence the work reported in this paper.

Acknowledgements

This project was supported by the National Natural Science Foundation of China (No. 11974300, 11974299 and 11704319), the Natural Science Foundation of Hunan Province (2021JJ30645, 2021JJ10036), the Scientific Research Fund of Hunan Provincial Education Department (No. 19B554, 20K127, 20A503 and 20B582), the Program for Changjiang Scholars and Innovative Research Team in University (IRT13093) and the Hunan Provincial Innovation Foundation for Postgraduate (No. CX20200624). Research reported in this publication was supported in part by the NSF (award number 2030128).

References

1 H. W. Kroto, J. R. Heath, S. C. O'Brien, R. F. Curl and R. E. Smalley, *Nature*, 1985, **318**, 162–163.
2 R. Baughman, H. Eckhardt and M. Kertesz, *J. Chem. Phys.*, 1987, **87**, 6687–6699.

 This journal is © The Royal Society of Chemistry 2021

3 S. Iijima, *Nature*, 1991, **354**, 56–58.
4 Y. P. Kudryavtsev, R. B. Heimann and S. E. Evsyukov, *J. Mater. Sci.*, 1996, **31**, 5557–5571.
5 K. S. Novoselov, A. K. Geim, S. V. Morozov, D.-E. Jiang, Y. Zhang, S. V. Dubonos, I. V. Grigorieva and A. A. Firsov, *Science*, 2004, **306**, 666–669.
6 A. Hirsch, *Nat. Mater.*, 2010, **9**, 868–871.
7 Z.-S. Wu, W. Ren, L. Gao, J. Zhao, Z. Chen, B. Liu, D. Tang, B. Yu, C. Jiang and H.-M. Cheng, *ACS Nano*, 2009, **3**, 411–417.
8 L. Lindsay, D. A. Broido and N. Mingo, *Phys. Rev. B: Condens. Matter Mater. Phys.*, 2010, **82**, 115427.
9 A. N. Enyashin and A. L. Ivanovskii, *Phys. Status Solidi B*, 2011, **248**, 1879–1883.
10 X.-Q. Wang, H.-D. Li and J.-T. Wang, *Phys. Chem. Chem. Phys.*, 2013, **15**, 2024–2030.
11 W.-J. Yin, Y.-E. Xie, L.-M. Liu, R.-Z. Wang, X.-L. Wei, L. Lau, J.-X. Zhong and Y.-P. Chen, *J. Mater. Chem. A*, 2013, **1**, 5341–5346.
12 X. Li, Q. Wang and P. Jena, *J. Phys. Chem. Lett.*, 2017, **8**, 3234–3241.
13 X. Wang, Z. Feng, J. Rong, Y. Zhang, Y. Zhong, J. Feng, X. Yu and Z. Zhan, *Carbon*, 2019, **142**, 438–444.
14 Q. Song, B. Wang, K. Deng, X. Feng, M. Wagner, J. D. Gale, K. Müllen and L. Zhi, *J. Mater. Chem. C*, 2013, **1**, 38–41.
15 S. Zhang, J. Zhou, Q. Wang, X. Chen, Y. Kawazoe and P. Jena, *Proc. Natl. Acad. Sci. U. S. A.*, 2015, **112**, 2372–2377.
16 J.-W. Jiang, J. Leng, J. Li, Z. Guo, T. Chang, X. Guo and T. Zhang, *Carbon*, 2017, **118**, 370–375.
17 B. Wu, X. Jia, Y. Wang, J. Hu, E. Gao and Z. Liu, *J. Mater. Chem. A*, 2019, **7**, 17357–17365.
18 C. Su, H. Jiang and J. Feng, *Phys. Rev. B: Condens. Matter Mater. Phys.*, 2013, **87**, 075453.
19 Z. Wang, X.-F. Zhou, X. Zhang, Q. Zhu, H. Dong, M. Zhao and A. R. Oganov, *Nano Lett.*, 2015, **15**, 6182–6186.
20 H. Yin, X. Shi, C. He, M. Martinez-Canales, J. Li, C. J. Pickard, C. Tang, T. Ouyang, C. Zhang and J. Zhong, *Phys. Rev. B*, 2019, **99**, 041405.
21 Z. Gong, X. Shi, J. Li, S. Li, C. He, T. Ouyang, C. Zhang, C. Tang and J. Zhong, *Phys. Rev. B*, 2020, **101**, 155427.
22 G. Li, Y. Li, H. Liu, Y. Guo, Y. Li and D. Zhu, *Chem. Commun.*, 2010, **46**, 3256–3258.
23 Q. Fan, D. Martin-Jimenez, D. Ebeling, C. K. Krug, L. Brechmann, C. Kohlmeyer, G. Hilt, W. Hieringer, A. Schirmeisen and J. M. Gottfried, *J. Am. Chem. Soc.*, 2019, **141**, 17713–17720.
24 Q. Fan, L. Yan, M. W. Tripp, O. Krejčí, S. Dimosthenous, S. R. Kachel, M. Chen, A. S. Foster, U. Koert and P. Liljeroth, *Science*, 2021, **372**, 852–856.
25 F. Q. Wang, J. Yu, Q. Wang, Y. Kawazoe and P. Jena, *Carbon*, 2016, **105**, 424–429.
26 P. H. Jiang, H. J. Liu, L. Cheng, D. D. Fan, J. Zhang, J. Wei, J. H. Liang and J. Shi, *Carbon*, 2017, **113**, 108–113.
27 M. Hu, K. P. Giapis, J. V. Goicochea, X. Zhang and D. Poulikakos, *Nano Lett.*, 2011, **11**, 618–623.
28 W.-L. Ong, E. S. O'Brien, P. S. M. Dougherty, D. W. Paley, C. Fred Higgs Iii, A. J. H. McGaughey, J. A. Malen and X. Roy, *Nat. Mater.*, 2017, **16**, 83–88.
29 L. Yang, N. Yang and B. Li, *Nano Lett.*, 2014, **14**, 1734–1738.
30 T. Ouyang, Q. Liu, M. Chen, C. Tang, J. Li, C. Zhang, C. He, H. Bao, J. Zhong and M. Hu, *ES Energy Environ.*, 2018, **3**, 88–95.
31 N. F. Hinsche, B. Y. Yavorsky, I. Mertig and P. Zahn, *Phys. Rev. B: Condens. Matter Mater. Phys.*, 2011, **84**, 165214.
32 G. Qin, Z. Qin, H. Wang and M. Hu, *Nano Energy*, 2018, **50**, 425–430.
33 P. Zhang, T. Ouyang, C. Tang, C. He, J. Li, C. Zhang and J. Zhong, *Phys. E*, 2020, **118**, 113870.
34 S.-K. Chien, Y.-T. Yang and C. O.-K. Chen, *Appl. Phys. Lett.*, 2011, **98**, 033107.
35 X. Wu, V. Varshney, J. Lee, T. Zhang, J. L. Wohlwend, A. K. Roy and T. Luo, *Nano Lett.*, 2016, **16**, 3925–3935.
36 P. E. Blöchl, *Phys. Rev. B: Condens. Matter Mater. Phys.*, 1994, **50**, 17953–17979.
37 G. Kresse and D. Joubert, *Phys. Rev. B: Condens. Matter Mater. Phys.*, 1999, **59**, 1758–1775.
38 J. Hafner, *J. Comput. Chem.*, 2008, **29**, 2044–2078.
39 J. P. Perdew, K. Burke and M. Ernzerhof, *Phys. Rev. Lett.*, 1996, **77**, 3865–3868.
40 A. Togo and I. Tanaka, *Scr. Mater.*, 2015, **108**, 1–5.
41 W. Li, L. Lindsay, D. A. Broido, D. A. Stewart and N. Mingo, *Phys. Rev. B: Condens. Matter Mater. Phys.*, 2012, **86**, 174307.
42 Z. Han, X. Yang, W. Li, T. Feng and X. Ruan, 2021, arXiv preprint, arXiv:2104.04895.
43 W. Li, J. Carrete, N. A. Katcho and N. Mingo, *Comput. Phys. Commun.*, 2014, **185**, 1747–1758.
44 H. P. Veeravenkata and A. Jain, *Carbon*, 2021, **183**, 893–898.
45 X. Shi, C. He, C. J. Pickard, C. Tang and J. Zhong, *Phys. Rev. B*, 2018, **97**, 014104.
46 Y. Liao, X. Shi, T. Ouyang, C. Zhang, J. Li, C. Tang, C. He and J. Zhong, *J. Phys. Chem. Lett.*, 2021, **12**, 8889–8896.
47 G. Xie, D. Ding and G. Zhang, *Adv. Phys.: X*, 2018, **3**, 1480417.
48 G. Xie, Z. Ju, K. Zhou, X. Wei, Z. Guo, Y. Cai and G. Zhang, *npj Comput. Mater.*, 2018, **4**, 21.
49 P.-Z. Jia, Y.-J. Zeng, D. Wu, H. Pan, X.-H. Cao, W.-X. Zhou, Z.-X. Xie, J.-X. Zhang and K.-Q. Chen, *J. Phys.: Condens. Matter*, 2019, **32**, 055302.
50 Y. Machida, N. Matsumoto, T. Isono and K. Behnia, *Science*, 2020, **367**, 309–312.
51 W. Kaim, B. Schwederski and A. Klein, *Bioinorganic Chemistry–Inorganic Elements in the Chemistry of Life: An Introduction and Guide*, John Wiley & Sons, 2013.